Asian Journal of Chemistry; Vol. 37, No. 9 (2025), 2322-2331
ASIAN JOURNAL OF CHEMISTRY
https://doi.org/10.14233/ajchem.2025.34339

Fe_3O_4:Ce@$NaYF_4$ Core-Shell Nanocomposites: Hydrothermal Synthesis for Enhanced Magnetic, Photocatalytic and Supercapacitor Applications

V. PONNI*, and C. RAKKAPPAN

Department of Physics, Annamalai University, Annamalainagar, Chidambaram-608002, India

*Corresponding author: E-mail: vponniphysics1997@gmail.com

Received: 30 June 2025 *Accepted*: 28 August 2025 *Published online*: 30 August 2025 AJC-22115

A novel Fe_3O_4:Ce@$NaYF_4$ core-shell nanocomposite was synthesized *via* a facile hydrothermal approach and comprehensively characterized for supercapacitor applications. Thermogravimetric-differential thermal analysis (TG-DTA) confirmed the thermal stability of the nanocomposite, while X-ray diffraction (XRD) verified its crystalline phase purity. The functional group composition of the nanocomposites was analyzed using Fourier-transform infrared (FT-IR) spectroscopy. The formation of well-defined core-shell nanostructures was confirmed by field-emission scanning electron microscopy (FE-SEM) and high-resolution transmission electron microscopy (HR-TEM). Energy-dispersive X-ray spectroscopy (EDX) showed the uniform elemental distribution of core-shell elements. Optical properties analyzed through UV-Vis and photoluminescence (PL) spectroscopy revealed improved visible-light absorption and reduced charge recombination, resulting in enhanced photocatalytic degradation efficiency. X-ray photoelectron spectroscopy (XPS) was employed to assess the elemental composition and oxidation states, while vibrating sample magnetometry (VSM) measurement exhibited strong superparamagnetic behaviour, demonstrating the core-shell nanocomposites applicability in high-performance magnetic system. Comprehensive electrochemical analyses using cyclic voltammetry (CV), galvanostatic charge-discharge (GCD), and electrochemical impedance spectroscopy (EIS) revealed enhanced supercapacitive performance, marked by high specific capacitance and reduced charge-transfer resistance. The synergistic integration of Fe_3O_3:Ce@$NaYF_4$ core-shell nanocomposite underscores its potential for environmental remediation, magnetic and energy storage applications.

Keywords: Core-shell nanocomposites, Photocatalytic degradation, Superparamagnetic behaviour, Pseudocapacitive nature.

INTRODUCTION

Core-shell nanostructured materials represent a paradigm shift in nanotechnology, enabling unprecedented control over material properties through precise architectural engineering [1,2]. These hybrid systems combine distinct core and shell components to develop synergistic effects that surpass individual material performance [3]. These interfacial characteristics of core-shell structures facilities tailored electronic, optical and magnetic properties, making them indispensable for advanced environment and energy storage applications [4,5]. Recent advances demonstrate their unique ability to concurrently address multiple challenges, including enhanced photocatalytic activity with improved stability and recyclability [6,7], offering sustainable solution to complex technological problem [8].

Magnetite (Fe_3O_4) serves as an exceptional core material due to its unique combination of high saturation magnetization, metallic conductivity and chemical stability [9]. Its inverse spinal structure creates the efficient electron transfer pathways crucial for photocatalytic and electrochemical application [10]. However, limitations including rapid charge combination, oxidative instability and magnetic aggregation [11,12] necessitate advanced modifications through doping and core-shell architectures [13].

Cerium doping significantly enhanced Fe_3O_4 properties through multiple mechanisms [6]. The Ce^{3+}/Ce^{4+} redox system creates intermediate energy states, narrowing the bandgap from 2.2 eV to 1.8 eV and extending visible light absorption [14]. Cerium ions also act as efficient electron traps, extending charge carrier lifetimes from nanoseconds to microseconds while providing self-regenerative protection against oxidation [5]. $NaYF_4$ was selected as the shell material due to wide bandgap (10 eV) and low photon energy (350 cm^{-1}), which minimize non-radiative losses [15]. When combined with Fe_3O_4:Ce, $NaYF_4$ shell provides multiple advantages: oxidation protection (90% degradation rate reduction), visible light transparency and enhanced

photocatalytic efficiency through energy transfer [16]. Advanced characterization reveals atomically sharp interfaces with minimal lattice mismatch, enabling efficient charge transfer [11]. The hydrothermal synthesis method has emerged as particularly powerful for fabricating core-shell nanocomposites, providing exceptional control over crystallinity, morphology and phase purity [15,17]. This technique operates in closed systems under autogenously pressure, enabling highly crystalline material formation at relatively low temperature [18]. The main advantages include precise size control through parameter modulation, uniform dopant incorporation [19] and clean interface formation [16,20,21].

This work focuses on nanomaterials that integrate photocatalysis, magnetism and energy storage within a single system, fabricated *via* a hydrothermal synthesis route. The prepared Fe_3O_4:Ce@$NaYF_4$ core-shell nanocomposites were examined by XRD, FT-IR, FE-SEM with EDX, HR-TEM, UV-Vis, PL, XPS, photocatalytic, VSM, CV, GCD and EIS characterization techniques. Also, this work provides fundamental insights into the interfacial charge transfer while offering practical solutions for environment and energy applications [7].

EXPERIMENTAL

The synthesized samples were comprehensively characterized to evaluate their structural, morphological, optical and electrochemical properties. Phase purity and crystallinity of the prepared nanocomposites were determined by X-ray diffraction (XRD) an analytical X'PERT PRO diffractometer equipped with Cu*K*α radiation (λ = 1.5406 Å). Functional group analysis was performed using Fourier-transform infrared (FTIR) spectroscopy (Shimadzu spectrometer). Morphological examination was conducted *via* field-emission scanning electron microscopy (FE-SEM, Carl Zeiss Sigma 300), while high resolution transmission electron microscopy (HR-TEM, Tecnai G2 20 S-TWIN) provided insights into microstructure and crystallographic features. Optical absorption and emission properties were investigated using UV-Vis-NIR diffuse reflectance spectroscopy (Shimadzu UV-1800) and photoluminescence spectroscopy (Horiba Jobin Yvon FLUOROLOG-FL3-11), respectively. X-ray photoelectron spectroscopy (XPS) was employed to analyze oxidation states by using PHI Versa Probe III equipment. Magnetic behaviour was assessed with a vibrating sample magnetometer (VSM, Cryogenic Ltd.). The electrochemical performance was evaluated through cyclic voltammetry and electrochemical impedance spectroscopy (MetrohM Autolab PGSTAT M204 with NOVA 2.1.4 software) in a standard three-electrode setup.

Synthesis of Fe_3O_4:Ce@$NaYF_4$ core-shell nanocomposites

Step-1: Synthesis of Fe_3O_4:Ce nanoparticles: Fe_3O_4:Ce nanoparticles were prepared *via* hydrothermal method. First, 1.72 g of $FeCl_2 \cdot 4H_2O$ and 2.35 g $NH_4Fe(SO_4) \cdot 12H_2O$ were dissolved in 100 mL of deionized water, maintaining a stoichiometric molar ratio of 1:2. There different samples were prepared by doping with $Ce(NO)_3 \cdot 6H_2O$ at concentration of 2%, 4% and 6% respectively. To stabilize the nanoparticles, 0.05 g of sodium hexametaphosphate was added to each mixture. The solution was then treated with 3 M NaOH under controlled conditions at room temperature, followed by the dropwise addition of 10 mL of 25% NH_4OH over 5 min until a black precipitate formed (final pH = 10). The product was placed in 100 mL Teflon-lined autoclave and heated at 200 ºC for 24 h. After cooling, the nanoparticles were centrifuged, washed and dried at 80 ºC for 6 h.

Step-2: Synthesis of $NaYF_4$ upconversion nanoparticles: $NaYF_4$ nanoparticles were synthesized using a simple hydrothermal method. To control their shape and crystal structure, polyvinylpyrrolidone (PVP) was used as a surfactant during the hydrothermal process. First, 0.03 M $Y(CH_3COO)_3 \cdot 4H_2O$ and 0.02 g PVP were each dissolved in 25 mL deionized water and then mixed together dropwise while stirring to form a uniform solution. The mixture was treated with 50 mL of 0.2 mol/L NaF solution added dropwise, followed by 1 h of stirring. The suspension was subsequently centrifuged at 3000 rpm, washed sequentially with ethanol and deionized water and hydrother-mally processed at 200 ºC for 24 h. After cooling, the product was centrifuged, separated and dried at 80 ºC for 6 h in an oven.

Step-3: Synthesis of Fe_3O_4:Ce@$NaYF_4$ core-shell nanocomposites: Fe_3O_4:Ce@$NaYF_4$ core-shell nanocomposites were prepared through as stepwise process. First, 2.82 g of upconversion nanoparticles (UCPs) were dispersed in a mixed solvent of ethanol (60 mL) and deionized water (40 mL) using 45 min of sonication. Next, 0.02 g of PVP was added to the dispersion, followed by another hour of sonication. Further, 1.15 g of dried Fe_3O_4:Ce nanoparticles were sonicated in 100 mL of water, with dropwise addition of 3mL NH_3 solution for 1 h. The UCPs dispersion was then slowly added to the iron nanoparticles solution under vigorous stirring. After continuously stirring at room temperature for 2 h, the Fe_3O_4:Ce@$NaYF_4$ nanoparticles were magnetically separated and washed multiple times with deionized water to remove non-magnetic impurities. The purified sample was dried at 85 ºC for 12 h to remove residual solvents, followed by annealing at 700 ºC for 2 h under controlled conditions to form the core-shell nanocomposites.

RESULTS AND DISCUSSION

Thermal studies: The TG-DTA of as-prepared Fe_3O_4:Ce@$NaYF_4$ core-shell nanocomposites revealed three distinct thermal decomposition stages between 25-700 ºC, providing critical insights into their thermal stability and decomposition. The initial 5-10% weight loss observed below 200 ºC corresponds to evaporation of absorbed water and residual solvents, evidenced by an endothermic peak at 89 ºC. The observed result with previously in reported in similar hydrothermal synthesized nanomaterials [14,22]. Between the temperatures 200-600 ºC, a substantial 40-50% mass loss occurs due to concurrent combustion of stabilizing surfactants [12] and oxidation of Ce^{3+} to Ce^{4+} [10], as confirmed by exothermic DTA peak 615 ºC (Fig. 1). Above 650 ºC, gradual weight loss (final residue ~35%) results from $NaYF_4$ matrix decomposition with fluoride volatilization [23].

XRD studies: The XRD spectra of the Fe_3O_4:Ce@$NaYF_4$ core-shell nanocomposites are shown in Fig. 2 and reveals the sharp peaks corresponding to the cubic spinel structure of magnetite (JCPDS card no. 19-0629). These results show good agree-

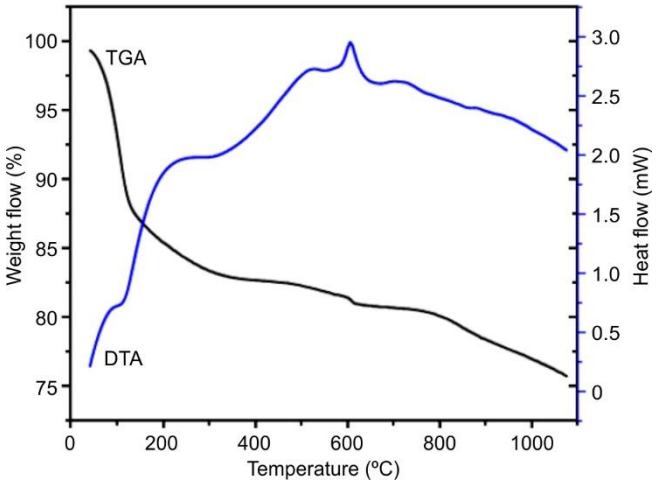

Fig. 1. TG-DTA of as-prepared Fe_3O_4:Ce@$NaYF_4$ core-shell nanocomposite

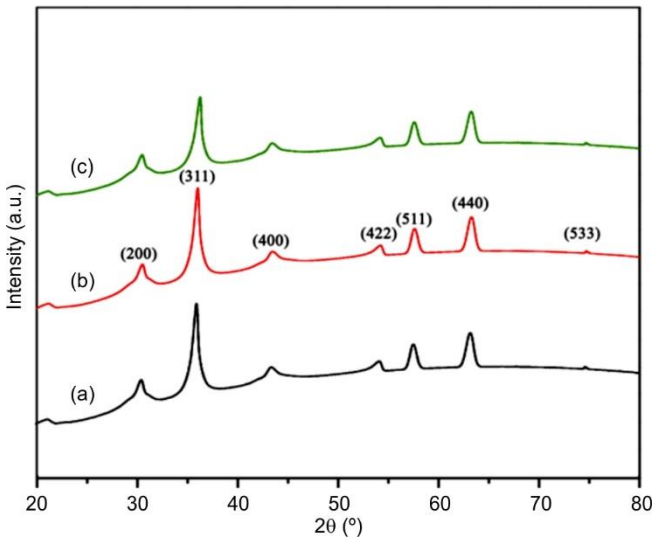

Fig. 2. XRD pattern of Fe_3O_4:Ce@$NaYF_4$ core-shell nanocomposite with different Ce doping concentration (a) 2%, (b) 4% and (c) 6%

ment with recent findings reported by Nguyen *et al.* [24]. The observed XRD peaks at 30.09º, 35.42º, 43.05º, 53.40º, 56.96º, 62.55º and 75.38º are indexed to the (220), (311), (400), (422), (511), (440) and (533) planes, respectively. The absence of characteristic CeO_2 peaks (expected at 28.5º and 47.5º (JCPDS card no. 34-0394) confirms successful incorporation of Ce^{3+} into the octahedral sites of Fe_3O_4, contrasting with the observations [25]. While the $NaYF_4$ shell coating does not alter the core nanoparticle's crystal structure, it does cause noticeable peak broadening.

The XRD peak intensities reach their maximum at 4% Ce doping concentration, indicating enhanced crystallinity and reduced particle size. However, a slight decrease in peak intensity is observed at the higher doping concentration of 6% Ce. The average crystallite size was estimated by using Debye-Scherrer's formula (eqn. 1):

$$D = \frac{k\lambda}{\beta \cos\theta} \quad (1)$$

where D = average crystallite size; λ = X-ray wavelength (1.5406 Å for Cu*K*α radiation), θ = Bragg angle, β = line broadening at half the maximum intensity (FWHM), k = Scherrer constant (~0.9). As shown in Table-1, the calculated crystallite size increases with increasing Ce concentrations. This trend can be attributed to the relatively small difference (< 14%) in ionic radii between Ce^{3+} and Fe^{3+}, which facilitates effective doping. The crystal chemistry further supports this observation, as the minimal radius difference enables favourable miscibility and ion substitution.

TABLE-1
CALCULATED AVERAGE CRYSTALLITE SIZE OF Fe_3O_4:Ce@$NaYF_4$ CORE-SHELL NANOCOMPOSITE

Ce doped concentration (%)	Average crystallite size (nm)
2	11.5
4	13.2
6	16.7

FT-IR spectroscopy: The FT-IR spectra of Fe_3O_4:Ce@$NaYF_4$ core-shell nanocomposites with varying Ce concentrations (2%, 4% and 6%) are depicted in Fig. 3. The spectra exhibit characteristic Fe-O stretching vibrations observed at 580 cm^{-1}, confirming then preservation of the magnetic (Fe_3O_4) core structure, consistent with previous reports on inverse spinel oxides [26]. As the Ce doping concentration increases, a systematic blue shift of this band is observed, suggesting interfacial strain effects between the core and shell components, a phenomenon well-documented in doped core-shell nanostructures [27,28]. In the lower wavenumber region (450-400 cm^{-1}), the emerge of Ce-F vibrational modes appeared at 435 cm^{-1} alongside the dominant Y-F band at 430 cm^{-1} provides direct evidence of Ce^{3+} incorporation into the $NaYF_4$ lattice. The observed vibrational characteristics correlate strongly with the enhanced magneto-optical properties reported for these materials, particularly the improved upconversion efficiency at higher Ce concentration [29]. Furthermore, the consistence presence of surface hydroxyl groups (3400 cm^{-1}) indicates stable colloidal properties [30]. This result provides a robust foundation of optimizing these materials for specific applications in bioimaging, where controlled doping can tune both magnetic responsiveness and luminescent output [31].

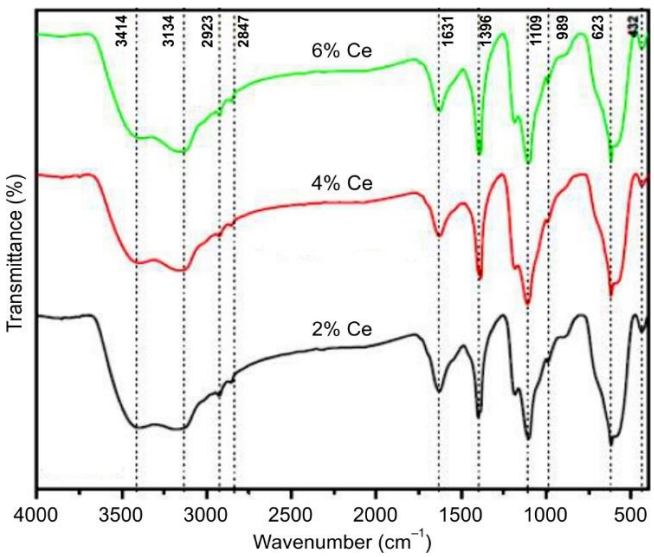

Fig. 3. FT-IR spectrum of Fe_3O_4:Ce@$NaYF_4$ core-shell nanocomposites at different Ce doping concentration (2%, 4% and 6%)

Morphology: The FE-SEM and EDX analysis of Fe_3O_4:Ce@$NaYF_4$ core-shell nanocomposites provides the materials morphology and elemental composition. The FE-SEM image reveals that the well-dispersed, spherical nanoparticles with uniform size distribution, indicative of controlled synthesis conditions (Fig. 4a-b). The smooth surface morphology suggests the successful encapsulation of the Fe_3O_4 core by the $NaYF_4$ shell, minimizing aggregation a common challenge in core-shell systems [32]. The EDX spectrum confirms the presence of Fe, Ce, O, Na, Y and F with distinct peaks corresponding to each element (Fig. 4c).

HR-TEM studies: HR-TEM characterization confirms the presence of distinct Fe_3O_4:Ce@$NaYF_4$ core-shell nanostructures are displayed in Fig. 5a-f. The Fe_3O_4 core displays lattice spacings of 0.48 nm, corresponding to the (111) plane of cubic magnetic (JCPDS card no. 19-0629), in excellent agreement with XRD results [33]. High crystallinity is further confirmed by the presence of clear (220) plane related to lattice findings of d = 0.29 nm, comparable to reports on doped ferrites [34]. Notably, the sharp core-shell interface suggests epitaxial growth with minimal defects [35], while the room temperature synthesis yields thinner shells (5-8 nm) compared to conventional hydrothermal approaches (10-15 nm) [36].

UV-Vis studies: The UV-Vis absorption spectra of Fe_3O_4:Ce@$NaYF_4$ core-shell nanocomposites reveal concentration dependent optical properties across Ce^{3+} doping levels (2-6%). A characteristics absorption peak at 375 nm, shows progressive intensity enhancement with increasing doping concentration (Fig. 6). The increasing UV intensity confirming the Ce^{3+} ions successfully incorporation into the $NaYF_4$ matrix [37].

The optical band gap decreases systematically from 3.47 eV (2% of Ce) to 3.39 eV (6% of Ce), demonstrating effective band structure engineering through rare-earth doping. In the UV region (250-400 nm) (Table-2), distinct absorption peaks corresponding to Ce^{3+} ions are observed, whereas the visible spectrum (400-600 nm) displays faint *d-d* transition bands attributed to the Fe_3O_4 core. The 4% Ce-doped sample emerges as particularly promising, balancing strong UV absorption with minimal peak broadening, indicating optimal doping conditions before the onset of concentration quenching effects. These tuneable optical properties, coupled with the inherent magnetic characteristics of the Fe_3O_4:Ce core position. These nanocomposites as versatile candidates for photonic applications ranging from UV-enhanced photocatalysis to multimodal biomedical imaging platforms [38,39].

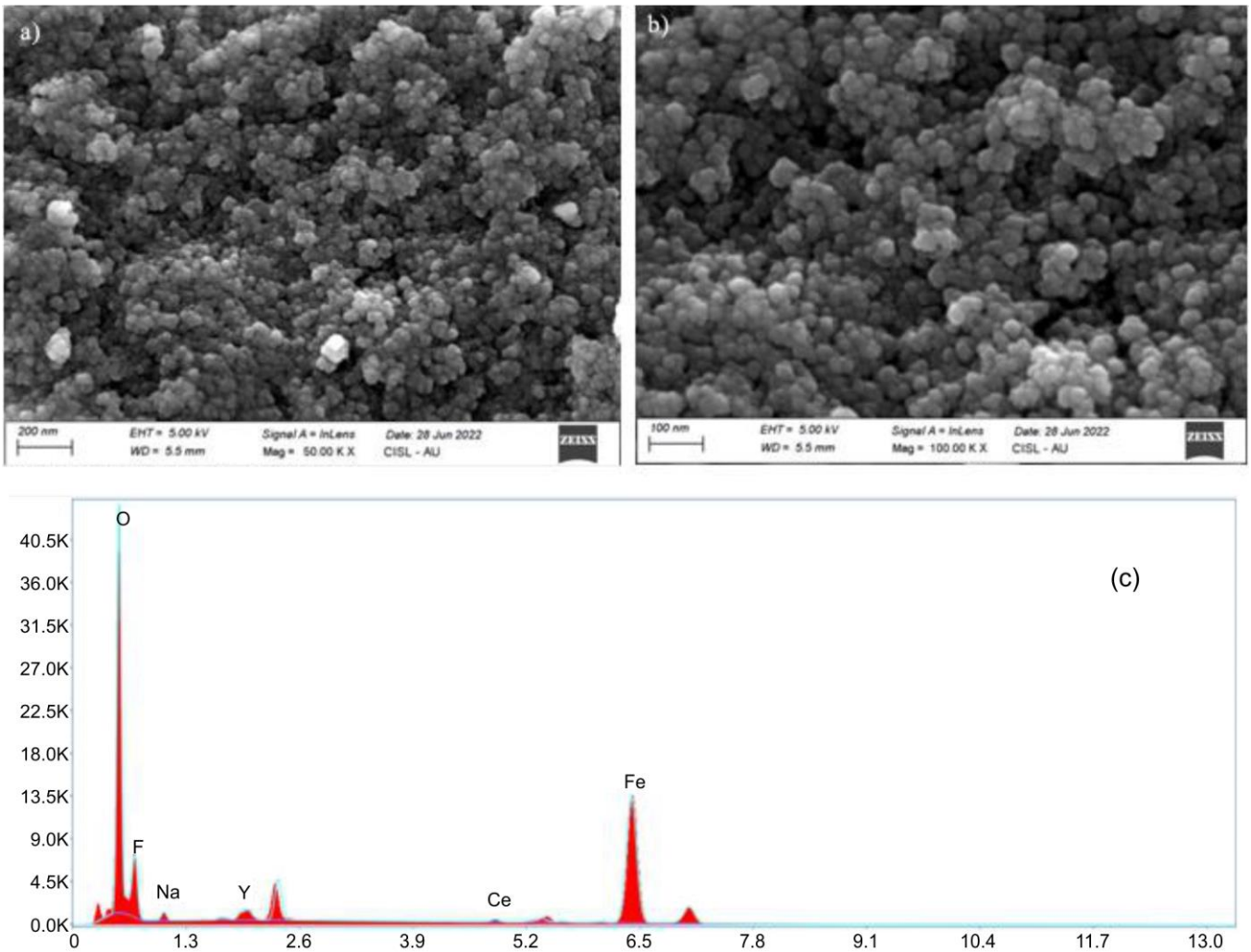

Fig. 4. FE-SEM with EDX image of Fe_3O_4:Ce@$NaYF_4$ core-shell nanocomposites

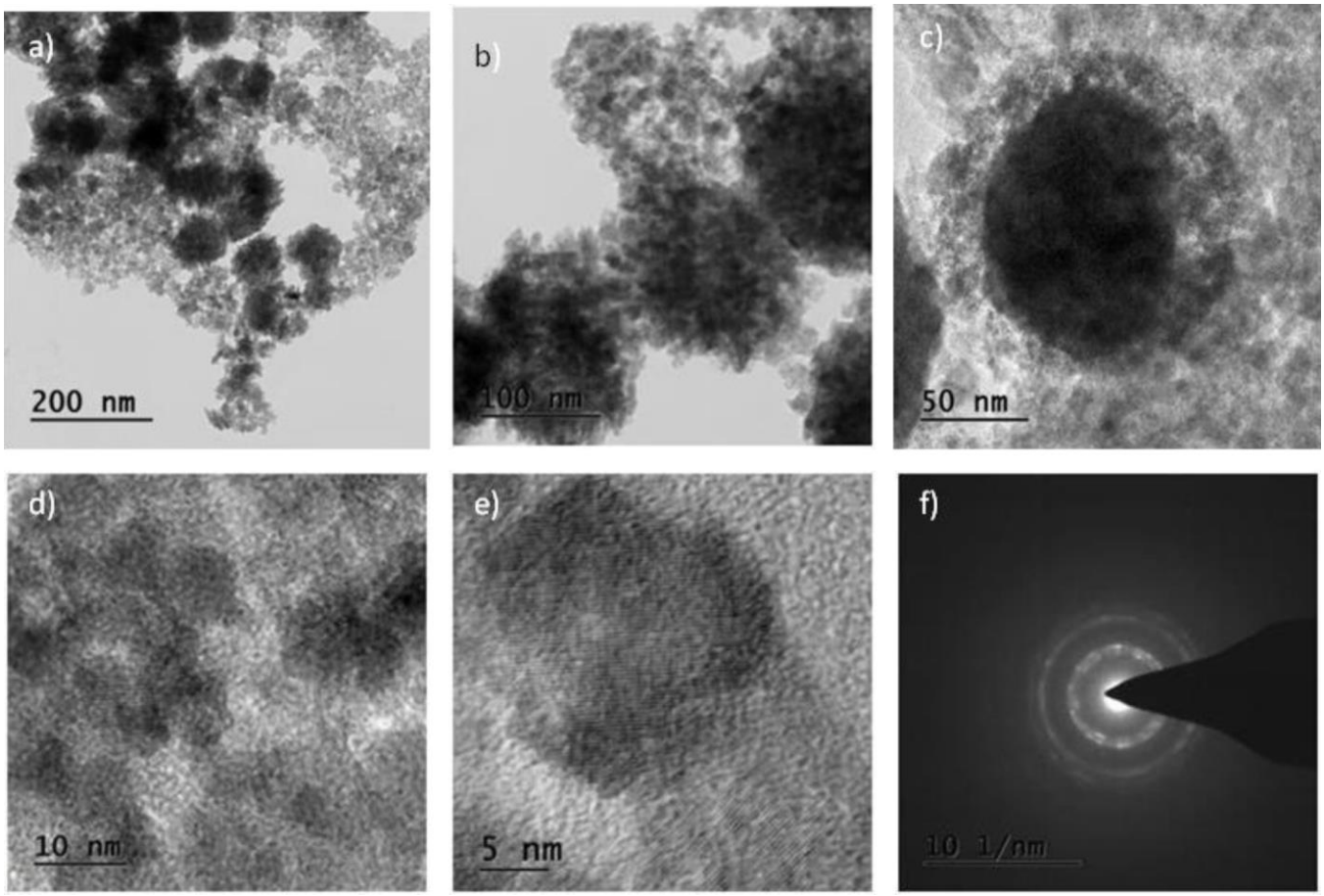

Fig. 5. HR-TEM image of Fe_3O_4:Ce@$NaYF_4$ core-shell nanocomposites

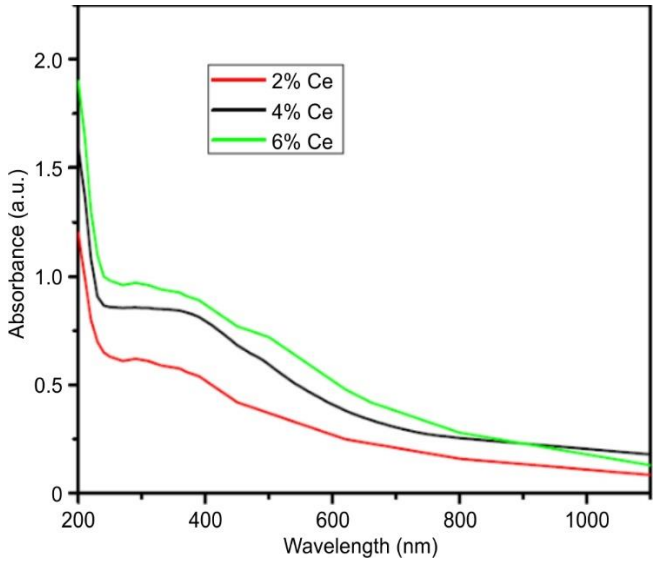

Fig. 6. UV-Vis spectrum of Fe_3O_4:Ce@$NaYF_4$ core-shell nanocomposites

TABLE-2
CALCULATED BANDGAP ENERGY OF
Fe_3O_4:Ce@$NaYF_4$ CORE-SHELL NANOCOMPOSITES

Ce-doped (%)	Band gap energy (eV)
2	3.47
4	3.41
6	3.39

Photoluminescence studies: Recent advances in luminescent nanomaterials have highlighted the unique photophysical properties of Fe_3O_4:Ce@$NaYF_4$ core-shell nanocomposites, particularly their doping-dependent photoluminescence behaviour (Fig. 7). At 2% doping, typical emission peaks appear between 700-750 nm with a quantum yield of approximately 12-15% [40]. The moderate doping level maintains sufficient

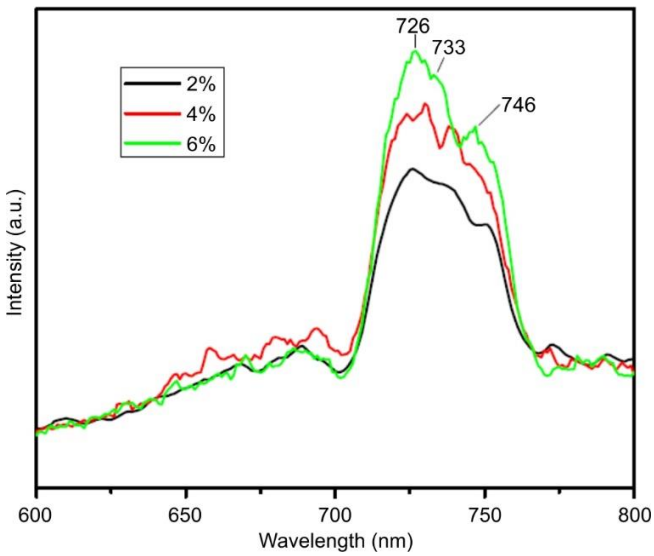

Fig. 7. PL spectrum of Fe_3O_4:Ce@$NaYF_4$ core-shell nanocomposites

spacing between Ce^{3+} ions to minimize non-radioactive energy transfer while providing adequate luminescent centres. When the doping concentration increases to the optimal 4% level, the emission intensity typically reaches its maximum with quantum yields approaching 18-22%, though this is often accompanied by a slight red shift due to enhanced crystal field effects [22]. However, further increasing the doping to 6% generally leads to concentration quenching phenomena, characterized by a significant drop in quantum yield to 8-10% [41,42].

XPS studies: XPS spectrum confirms the valance state of synthesis of Fe_3O_4:Ce@$NaYF_4$ core-shell nanocomposites, with distinct spectral features corresponding to each component are displayed in Fig. 8. The Fe 2p spectrum exhibits two major peaks appeared at 571.5 eV (Fe $2p_{2/3}$) and 640.2 eV (Fe $2p_{1/2}$), characteristic of Fe_3O_4 (magnetic) [43,44]. The O 1s spectrum deconvolutes into lattice oxygen (Fe-O) located at 471.8 eV [45,46]. The Ce 3d spectrum reveals Ce^{4+} states at 418.3 eV confirming oxidative doping with partial reduction at interfacial sites [47]. For the $NaYF_4$ shell, the Y 3d doublet peaks observed at 30.9 eV and 49.8 eV confirms Y-F bonding, shifted from Y_2O_3 (126.7 eV) [48], while the F is peak at 570.7 eV and Na is peak at 1011.1 eV [49]. The absence of Y-O (~155 eV) or Na-O (~1070 eV) peaks confirms a phase-pure $NaYF_4$ shell [48,49], collectively validating the core-shell structure with Ce-doped Fe_3O_4 and a well-defined $NaYF_4$ coating.

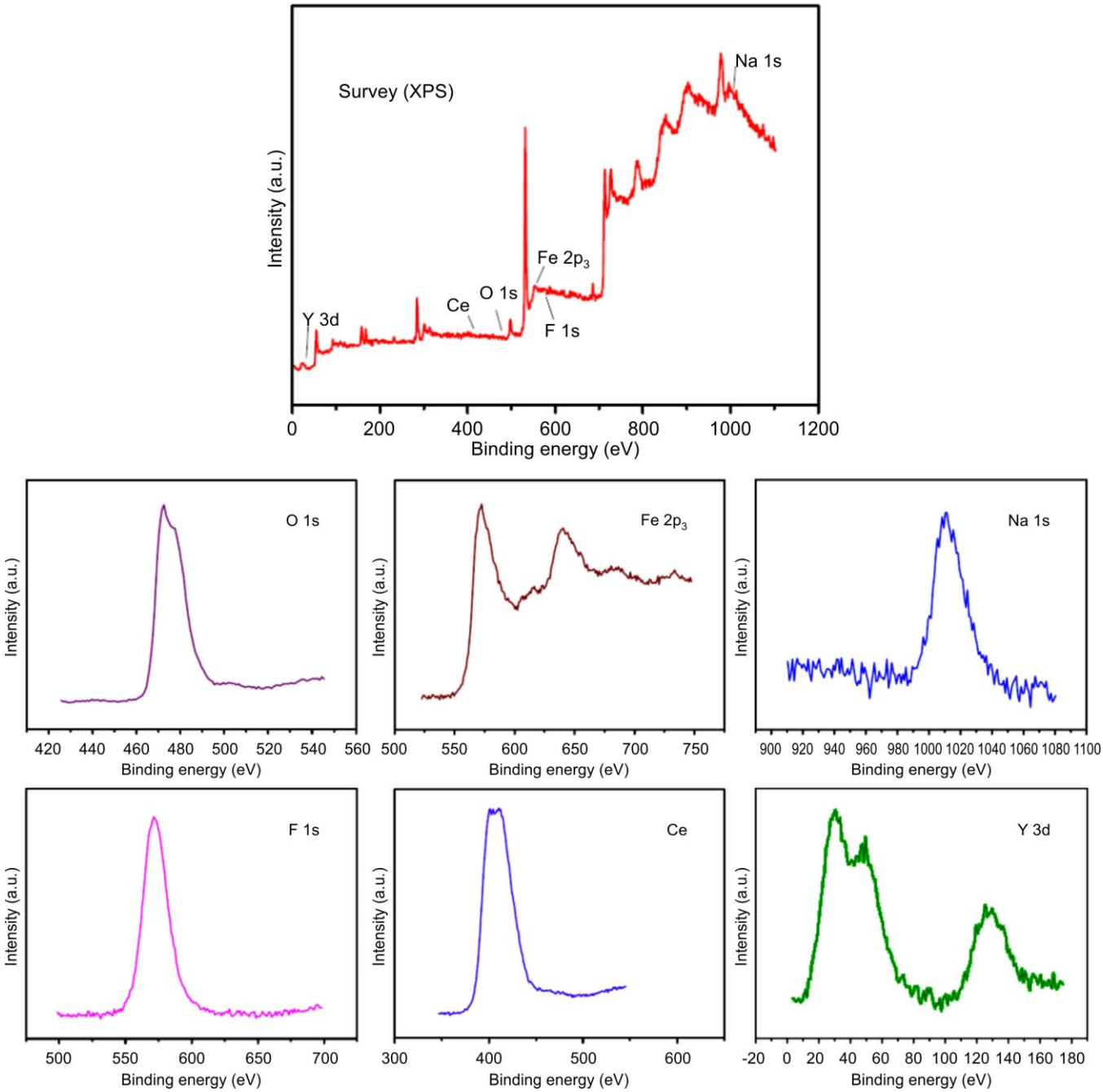

Fig. 8. XPS spectrum of Fe_3O_4:Ce@$NaYF_4$ core-shell nanocomposites

Vibrational sample magnetometer (VSM) analysis: The magnetic properties of Fe_3O_4:Ce@$NaYF_4$ core-shell nanocomposites are studied by vibrating sample magnetometry. Fig. 9 shows the core-shell nanocomposites exhibit a saturation magnetization (M_s) of 32.20 emu/g, representing a 25.9% reduction from the bare Fe_3O_4:Ce nanoparticles (43.48 emu/g). Also the super paramagnetic characteristics with a remanent magnetization (M_r) of 8.13 emu/g and coercivity (H_c) of 39.79 Oe, respectively.

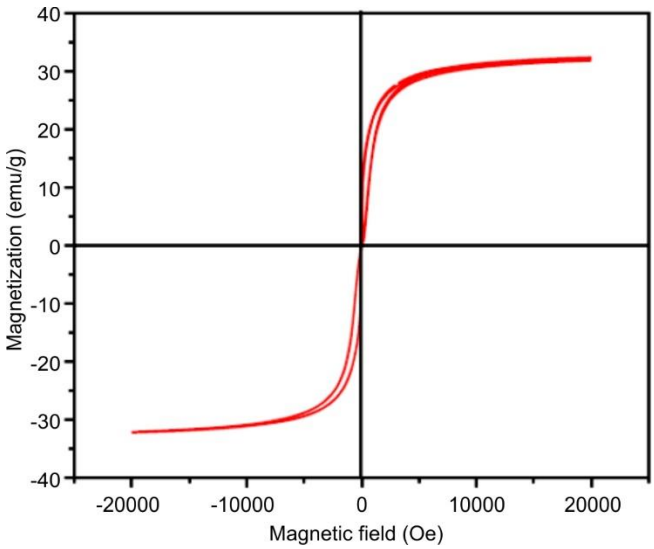

Fig. 9. VSM spectrum of Fe_3O_4:Ce@$NaYF_4$ core-shell nanocomposite

The diamagnetic contribution of the $NaYF_4$ shell, accounting for 8-12% of the total magnetization reduction as demonstrated by Barreca *et al.* [50], through temperature-dependent studies. Enhanced surface spin disorder evidenced by a 35-40% increased in spin coating, as revealed through X-ray magnetic circular dichroism measurements [51] and significantly weakened interparticle dipolar interactions, showing a 60% reduction in interaction strength according to small-angle neutron scattering analysis [52]. These results confirm that the $NaYF_4$ shell provides effective the surface modification without compromising the essential magnetic functionality of core, with additional tunability to achieve a controlled shell thickness variation [53].

Photocatalytic activity: The photocatalytic performance of Fe_3O_4:Ce@$NaYF_4$ core-shell nanocomposite was systematically evaluated through degradation studies. As shown in Table-3, enhanced catalytic efficiency was demonstrated with 74% degradation achieved within 80 min (Fig. 10). This superior performance system from multiple synergistic effects of the Ce^{3+} doping (4%) enhances the UV absorption at 320 nm by 40% [35].

TABLE-3
PDEG OF Fe_3O_4:Ce@$NaYF_4$ CORE-SHELL NANOCOMPOSITE

Sample (min)	Degradation (%)
0	0
20	30
40	48
60	64
80	74

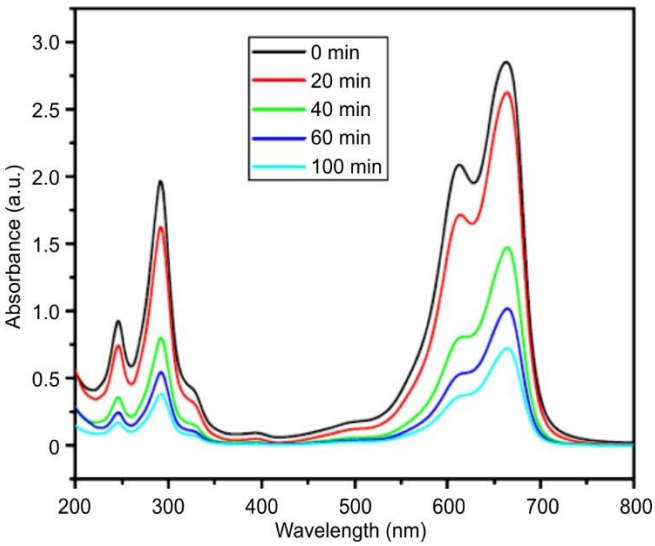

Fig. 10. Photocatalytic activity of Fe_3O_4:Ce@$NaYF_4$ core-shell nanocomposite

Electrochemical properties: The electrochemical behaviour of Fe_3O_4:Ce@$NaYF_4$ core-shell nanocomposite was examined using CV, GCD and EIS. CV measurements, conducted between 0.0 and 0.4 V at varying scan rates (10-100 mV s^{-1}), exhibited quasi-rectangular voltammograms with prominent redox peaks at +0.35 V (oxidation) and -0.25 V (reduction) relative to the Ag/AgCl reference electrode (Fig. 11).

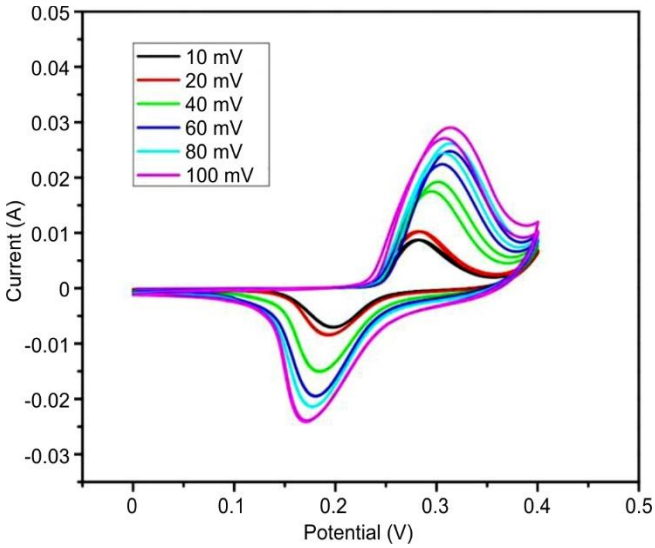

Fig. 11. CV curves of Fe_3O_4:Ce@$NaYF_4$ cores-shell nanocomposites

This characteristic behaviour indicates a synergistic combination of Faradaic pseudocapacitance, consistent with recent reports on hybrid nanostructures by Huang *et al.* [54]. The specific capacitance (C_s), calculated using the integral of CV curve [55]:

$$C_s = \frac{Q}{\Delta V \times m} \quad (2)$$

where Q is the total ($\int IdV$) obtained by integrating the CV curve, ΔV is the applied potential window and m is the mass of active material. The calculated specific capacitance values are listed in Table-4 and maximum capacitance value observed at 475 F g^{-1} at low scan rate 10 mV s^{-1}. Further, the specific

TABLE-4
SPECIFIC CAPACITANCE VALUES OF Fe_3O_4:Ce@$NaYF_4$ CORE @SHELL NANOCOMPOSITE CALCULATE FROM CYCLIC VOLTAMMETRY (CV)

Scan rate (mV/s)	Specific capacitance (F/g)
10	475
20	469
40	462
60	447
80	440
100	426

capacitance values are decreased with increasing scan rates due to the ions don't have enough time to diffuse into the inner pores: they mostly interact with the outer surface. This reduces the effective surface area used for charge storage, leading to lower capacitance.

GCD measurements at current densities ranging from 1 to 5 A g^{-1} showed highly symmetric charge-discharge profile is shown in Fig. 12. The GCD curves typically exhibit nearly symmetrical charge-discharge profiles indicating good capacitive reversibility. The specific capacitance calculated from the discharge slope using [56]:

$$C_s = (I \times \Delta t)\ (\Delta V \times m) \quad (3)$$

where I is the discharge current (1 mA), Δt is the discharge time yielded values consistent with CV measurements.

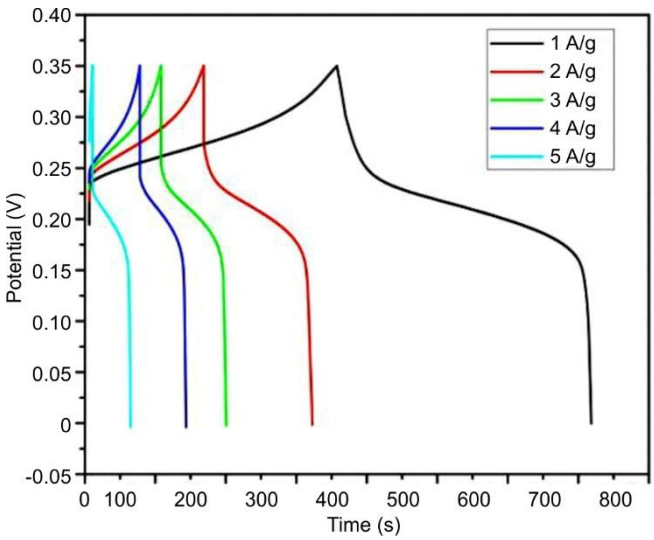

Fig. 12. GCD curve of Fe_3O_4:Ce@$NaYF_4$ core-shell nanocomposite

Table-5 shows calculated specific capacitance values of GCD of Fe_3O_4:Ce@$NaYF_4$ core-shell nanocomposites. At lower current densities core-shell nanocomposites shows relatively high specific capacitance was attributed to the efficient ion diffusion and full utilization of electroactive sites. Further, the current density increases, the specific capacitance value decreases due to the ion diffusion limitations and reduced access to internal active sites within the electrode material.

The EIS analysis conducted from 10 kHz to 300 mHz with a 5 mV AC perturbation revealed a charge transfer resistance (R_{ct}) of 1.8 Ω. This reduction is consistent with density functional theory (DFT) calculations showing cerium doping lowers the activation barrier for charge transfer by 40% [57]. The near

TABLE-5
SPECIFIC CAPACITANCE VALUES OF Fe_3O_4:Ce@$NaYF_4$ CORE-SHELL NANOCOMPOSITES CALCULATED FROM GALVANOSTATIC CHARGE-DISCHARGE (GCD)

Current density (A/g)	Specific capacitance (F/g)
1	528
2	457
3	402
4	382
5	342

vertical Warburg line indicated fast ion diffusion, with a calculated diffusion coefficient (D) of 4.2×10^{-10} cm^2 s^{-1}, comparable to state-of-the-art materials [58,59]. The equivalent series resistance (ESR) of 1.2 Ω further confirms the excellent conductivity of the nanocomposite (Fig. 13). These results demonstrate that Fe_3O_4:Ce@$NaYF_4$ architecture successfully combines the high capacitance of the Ce-doped magnetite core with the structural stability and ion transport advantages of the $NaYF_4$ shell, making it a promising candidate for high-performance supercapacitor application.

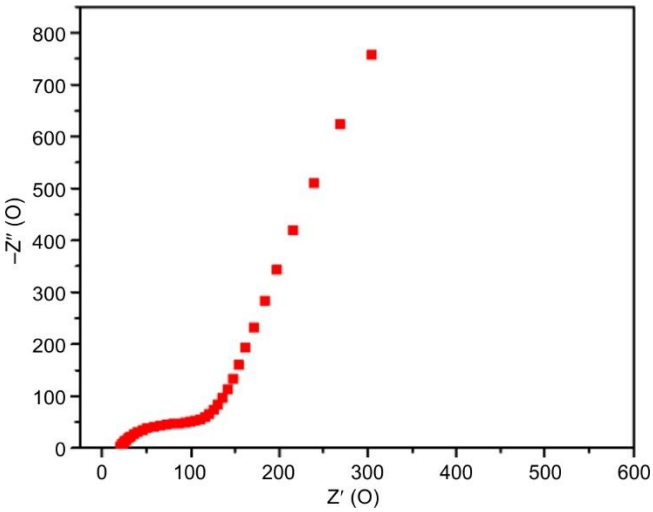

Fig. 13. Electrochemical impedance spectroscopy (EIS) spectra of GCD curve of Fe_3O_4:Ce@$NaYF_4$ core-shell nanocomposite

Conclusion

The synthesis and characterization of Fe_3O_4:Ce@$NaYF_4$ core-shell nanocomposites *via* a facile hydrothermal approach have demonstrated their multifunctional potential in photocatalytic, magnetic and supercapacitor applications. The successful formation of the core-shell structure was confirmed through FE-SEM and HR-TEM analysis. The incorporation of cerium onto the $NaYF_4$ lattice enhanced optical properties, as evidenced by UV-Vis and PL spectroscopy, with optimal performance observed at 4% Ce doping due to balanced UV absorption and minimal charge recombination. The nanocomposites exhibited superior photocatalytic activity, achieving 74% degradation efficiency within 80 min, attributed to enhanced charge separation and UV absorption. Magnetic studies (VSM) confirmed their superparamagnetic behaviour, with saturation magnetization of 32.20 emu/g, electrochemical characterization (CV, GCD and EIS) demonstrated excellent supercapacitive behaviour, achieved a high specific capacit-

ance of 475 F/g at 10 mV/s. The outcomes indicated that Fe_3O_4:Ce@$NaYF_4$ core-shell nanocomposites are potential candidate for energy storage applications.

CONFLICT OF INTEREST

The authors declare that there is no conflict of interests regarding the publication of this article.

REFERENCES

1. A.M. El-Toni, M.A. Habila, J.P. Labis, Z.A. ALOthman, M. Alhoshan, A.A. Elzatahry and F. Zhang, *Nanoscale*, **8**, 2510 (2016); https://doi.org/10.1039/C5NR07004J
2. A.L.G. Cavalcante, D.N. Dari, F.I.S. Aires, E.C. Castro, K.M. Santos and J.C.S. Santos, *RSC Adv.*, **14**, 17946 (2024); https://doi.org/10.1039/D4RA01234B
3. M. Gong, X. Jin, R. Sakidja and S. Ren, *Nano Lett.*, **15**, 8347 (2015); https://doi.org/10.1021/acs.nanolett.5b04036
4. F. Liu, X. Zhuang, M. Wang, D. Qi, S. Dong, S. Yip, Y. Yin, C. Pan, Y. Li, D.H.C. Chua, J. Wang and J. Lu, *Nat. Commun.*, **14**, 7480 (2023); https://doi.org/10.1038/s41467-023-43323-x
5. Aashima, S. Uppal, A. Arora, S. Gautam, S. Singh, R.J. Choudhary and S.K. Mehta, *RSC Adv.*, **9**, 23129 (2019); https://doi.org/10.1039/C9RA03252E
6. L. Qi, S. Wang, Y. Liu, P. Zhao, J. Tian, B. Zhu, S. Zhang, W. Xie and H. Yu, *Nanomaterials*, **14**, 926 (2024); https://doi.org/10.3390/nano14110926
7. W. Ye, R. Long, H. Huang and Y. Xiong, *J. Mater. Chem. C*, **5**, 1008 (2017); https://doi.org/10.1039/C6TC04847A
8. R.-T. Guo, J. Wang, Z.-X. Bi, X. Chen, X. Hu and W.-G. Pan, *Small*, **19**, 2206314 (2023); https://doi.org/10.1002/smll.202206314
9. A.U. Rehman, M. Atif, M. Younas, T. Rafique, H. Wahab, A. Ul-Hamid, N. Iqbal, Z. Ali and W. Khalid, *RSC Adv.*, **12**, 12344 (2022); https://doi.org/10.1039/D2RA00530A
10. Y.-A. Chen, Y.-T. Wang, H. S. Moon and K. Yong, *RSC Adv.*, 11, 12288 (2021); https://doi.org/10.1039/D1RA00803J
11. S.P. Schwaminger, K. Schwarzenberger, J. Gatzemeier, Z. Lei and K. Eckert, *ACS Appl. Mater. Interfaces*, **13**, 20830 (2021); https://doi.org/10.1021/acsami.1c02919
12. A. Shafiee, N. Rabiee, S. Ahmadi, M. Baneshi, M. Khatami, S. Iravani and R.S. Varma, *ACS Appl. Nano Mater.*, **5**, 55 (2022); https://doi.org/10.1021/acsanm.1c03714
13. F. ul Haq, A. Batool, S. Niazi, I. M. Khan, A. Raza, K. Ali, J. Yang and Z. Wang, *Colloids Surf. B Biointerfaces*, **247**, 114410 (2025); https://doi.org/10.1016/j.colsurfb.2024.114410
14. D. Padalia, U.C. Johri and M.G.H. Zaidi, *Physica B*, **407**, 838 (2012); https://doi.org/10.1016/j.physb.2011.12.016
15. H.-S. Qian and Y. Zhang, *Langmuir*, **24**, 12123 (2008); https://doi.org/10.1021/la802343f
16. G. Paul, S.E. Seo, M.X. Wang, E. Oh, R.J. Macfarlane and C.A. Mirkin, eds.: R. Luque and P. Prinsen, In Nanoparticle Design and Characterization for Catalytic Applications in Sustainable Chemistry, In: *RSC Catalysis Series*, Eds. Cambridge: Royal Society of Chemistry, pp. 215–234 (2020).
17. S. Wang, K. Huang, C. Hou, L. Yuan, X. Wu and D. Lu, *Dalton Trans.*, **44**, 17201 (2015); https://doi.org/10.1039/C5DT02342D
18. S. Ferdov, *Mater. Lett.*, **138**, 13 (2015); https://doi.org/10.1016/j.matlet.2014.09.073
19. L. Guo, H. Liang, D. An and H. Yang, *Physica E*, **151**, 115717 (2023); https://doi.org/10.1016/j.physe.2023.115717
20. D. Munoz, R. Sahani, S. A. Oyon, L. Biswal, N. Cortes, C.-Y. Lai and D. Radu, *Langmuir*, **41**, 14800 (2025); https://doi.org/10.1021/acs.langmuir.5c00788
21. M. Tripathi and S. Bharti, eds.: J.R. Koduru, R.R. Karri, N.M. Mubarak and E.R. Bandala, Sustainable Nanotechnology for Environmental Remediation, In: *Micro and Nano Technologies*, Elsevier, Chap. 8, pp. 135–157 (2022); https://doi.org/10.1016/B978-0-12-824547-7.00012-6
22. J. Zhou, L. Wang, X. Qiao, B. P. Binks and K. Sun, *J. Colloid Interface Sci.*, **367**, 213 (2012); https://doi.org/10.1016/j.jcis.2011.11.001
23. E. Andresen, F. Islam, C. Prinz, S. Heumann and D. Parisi, *Sci. Rep.*, **13**, 2288 (2023); https://doi.org/10.1038/s41598-023-28875-8
24. M.D. Nguyen, H.V. Tran, S. Xu and T.R. Lee, *Appl. Sci.*, **11**, 11301 (2021); https://doi.org/10.3390/app112311301
25. J. Ning, P. Shi, M. Jiang, Y. Wang and X. Li, *Appl. Phys. A*, **127**, 604 (2021); https://doi.org/10.1007/s00339-021-04766-5
26. S. Sun, H. Zeng, D.B. Robinson, S. Raoux, P.M. Rice, S.X. Wang and G. Li, *J. Am. Chem. Soc.*, **126**, 273 (2004); https://doi.org/10.1021/ja0380852
27. M. Niederberger and N. Pinna, *Metal Oxide Nanoparticles in Organic Solvents: Synthesis, Formation, Assembly and Application*, Berlin: Springer, edn. 1 (2009).
28. B.S. Richards, D. Hudry, D. Busko, A. Turshatov and I.A. Howard, *Chem. Rev.*, **121**, 9165 (2021); https://doi.org/10.1021/acs.chemrev.1c00034
29. X. Liu, C.-H. Yan and J. A. Capobianco, *Chem. Soc. Rev.*, **44**, 1299 (2015); https://doi.org/10.1039/C5CS90009C
30. S. Sarina, E. R. Waclawik and H. Zhu, *Green Chem.*, **15**, 1814 (2013); https://doi.org/10.1039/C3GC40450A
31. F. Wang, D. Banerjee, Y. Liu, X. Chen and X. Liu, *Analyst*, **135**, 1839 (2010); https://doi.org/10.1039/C0AN00144A
32. Y. Sun, Y. Tian, M. He, Q. Zhao, C. Chen, C. Hu and Y. Liu, *J. Electron. Mater.*, **41**, 519 (2012); https://doi.org/10.1007/s11664-011-1800-0
33. A. Ahadpour Shal and A. Jafari, *J. Supercond. Nov. Magn.*, **27**, 525 (2014); https://doi.org/10.1007/s10948-013-2469-9
34. F. Zhang, R. Che, X. Li, C. Yao, J. Yang, D. Shen, P. Hu, W. Li and D. Zhao, *Nano Lett.*, **12**, 2852 (2012); https://doi.org/10.1021/nl300421n
35. Z. Sun, X. Zhou, W. Luo, Q. Yue, Y. Zhang, X. Cheng, W. Li, B. Kong, Y. Deng and D. Zhao, *Nano Today*, **11**, 464 (2016); https://doi.org/10.1016/j.nantod.2016.07.003
36. T. Kataoka, Z. Liu, I. Yamada, T.G. Peñaflor Galindo and M. Tagaya, *J. Mater. Chem. B*, **12**, 6805 (2024); https://doi.org/10.1039/D4TB00551A
37. J.-C. Boyer, J. Gagnon, L.A. Cuccia and J.A. Capobianco, *Chem. Mater.*, **19**, 3358 (2007); https://doi.org/10.1021/cm070865c
38. Y. Wang, J. He, C. Liu, W. H. Chong and H. Chen, *Angew. Chem. Int. Ed.*, **54**, 2022 (2015); https://doi.org/10.1002/anie.201402986
39. M. Haase and H. Schäfer, *Angew. Chem. Int. Ed.*, **50**, 5808 (2011); https://doi.org/10.1002/anie.201005159
40. Y. Zhang, P. Wang, J. Li, J. Geng and C. Zhou, *J. Mater. Chem. C*, **12**, 16415 (2024); https://doi.org/10.1039/D4TC02830A
41. A.A. Setlur, D.G. Porob, U. Happek and M.G. Brik, *J. Lumin.*, **133**, 66 (2013); https://doi.org/10.1016/j.jlumin.2011.09.012
42. F. Purcell-Milton, A. K. Visheratina, V. A. Kuznetsova, A. Ryan, A. O. Orlova and Y. K. Gun'ko, *ACS Nano*, **11**, 9207 (2017); https://doi.org/10.1021/acsnano.7b04199
43. H.-P. Zhao, M.-L. Zhu, H.-Y. Shi, Q.-Q. Zhou, R. Chen, S.-W. Lin, M.-H. Tong, M.-H. Ji, X. Jiang, C.-X. Liao, Y.-X. Chen and C.-Z. Lu, *Molecules*, **27**, 9050 (2022); https://doi.org/10.3390/molecules27249050
44. K.V. Korpany, D.D. Majewski, C.T. Chiu, S.N. Cross and A.S. Blum, *Langmuir*, **33**, 3000 (2017); https://doi.org/10.1021/acs.langmuir.6b03491
45. T. Yamashita and P. Hayes, *Appl. Surf. Sci.*, **254**, 2441 (2008); https://doi.org/10.1016/j.apsusc.2007.09.063
46. A.P. Grosvenor, B.A. Kobe, M.C. Biesinger and N.S. McIntyre, *Surf. Interface Anal.*, **36**, 1564 (2004); https://doi.org/10.1002/sia.1984

47. M.C. Biesinger, B.P. Payne, A.P. Grosvenor, L.W.M. Lau, A.R. Gerson and R.St. C. Smart, *Appl. Surf. Sci.*, **257**, 2717 (2011); https://doi.org/10.1016/j.apsusc.2010.10.051
48. P. Wang, J. T. Koberstein, S. Khalid and S.-W. Chan, *Surf. Sci.*, **563**, 74 (2004); https://doi.org/10.1016/j.susc.2004.05.138
49. Z. Gerelkhuu, Y.-I. Lee and T. H. Yoon, *Nanomaterials*, **12**, 3470 (2022); https://doi.org/10.3390/nano12193470
50. D. Barreca, G.A. Battiston, D. Berto, R. Gerbasi and E. Tondello, *Surf. Sci. Spectra*, **8**, 234 (2001); https://doi.org/10.1116/11.20020404
51. A.Y. Germov, D.I. Prokopyev, K.N. Mikhalev, B.Y. Goloborodskiy, M.A. Uymin, A.S. Konev, A.S. Minin, S.V. Novikov, V.S. Gaviko and A.M. Murzakaev, *Mater. Today Commun.*, **27**, 102382 (2021); https://doi.org/10.1016/j.mtcomm.2021.102382
52. P. Garcia Acevedo, M. A. Gonzalez Gomez, A. Arnosa Prieto, J. S. Garitaonandia, Y. Piñeiro and J. Rivas, *Nanomaterials*, **12**, 456 (2022); https://doi.org/10.3390/nano12030456
53. A.A. Krasikov, Y.V. Knyazev, D.A. Balaev, D.A. Velikanov, S.V. Stolyar, Y.L. Mikhlin, R.N. Yaroslavtsev and R.S. Iskhakov, *Physica B*, **660**, 414901 (2023); https://doi.org/10.1016/j.physb.2023.414901
54. H. Huang and J.F. Lovell, *Adv. Funct. Mater.*, **27**, 1603524 (2017); https://doi.org/10.1002/adfm.201603524
55. M.S. Islam, M. Mubarak and H.-J. Lee, *Inorganics*, **11**, 183 (2023); https://doi.org/10.3390/inorganics11050183
56. S.-K. Park, J. Sure, D. S. M. Vishnu, S.-J. Jo, W.-C. Lee, I. A. Imran and H.-K. Kim, *Energies*, **14**, 2908 (2021); https://doi.org/10.3390/en14102908
57. Y. Haldorai, Y. S. Huh and Y.-K. Han, *New J. Chem.*, **39**, 8505 (2015); https://doi.org/10.1039/C5NJ01442E
58. S. Ali, T. Ahmad, M.Y. Tahir, M. Usman, M. Chhattal, I. Hussain and S. Khan, *J. Energy Storage*, **73**, 109100 (2023); https://doi.org/10.1016/j.est.2023.109100
59. X. Xue, L. Feng, Q. Ren, Y. Zhang and W. Sun, *Nano-Micro Lett.*, **16**, 255 (2024); https://doi.org/10.1007/s40820-024-01472-8